Atmos. Meas. Tech. Discuss., 5, 1075–1100, 2012
www.atmos-meas-tech-discuss.net/5/1075/2012/
doi:10.5194/amtd-5-1075-2012

Atmospheric Measurement Techniques Discussions

Temperature profiles with bi-static Doppler-RASS and their accuracy

B. Hennemuth[1], **G. Peters**[2], **and H.-J. Kirtzel**[2]

[1]Consulting Meteorologist, Hamburg, Germany
[2]METEK Meteorologische Messtechnik GmbH, Elmshorn, Germany

Received: 2 December 2011 – Accepted: 20 January 2012 – Published: 3 February 2012

Correspondence to: B. Hennemuth (barbara.hennemuth@zmaw.de)

Published by Copernicus Publications on behalf of the European Geosciences Union.

Abstract

The technique of atmospheric temperature profiling by Doppler-RASS is discussed. The set up with bi-static (separated transmit and receiving) antennas implies a range dependent scattering angle. The retrieval scheme developed by Kon for such antenna geometry is reviewed and its limits of validity are discussed. Empirical tuning of the efficient antenna aperture is proposed to fit the retrieved temperature profiles to reality. Examples of application of the measuring technique for atmospheric boundary layer characterization are presented.

1 Introduction

Temperature profiling in the lower troposphere is of great importance for several applications, e.g. for air pollution dispersion issues, determination of boundary layer height and of stratification in the mixing layer, or climatology of temperature profiles beyond 2 m which is needed for validation of atmospheric models. For such applications continuous measurements of temperature gradients are needed. While atmospheric stability is treated as a global variable in traditional routine air quality monitoring concepts, modern numerical models are able to account for the real local nature of stability and can accomodate even complex temperature profiles. RASS (Radio Acoustic Sounding System) has proven to be an adequate measuring system for high resolution temperature profiles in various atmospheric height ranges depending on the design characteristics.

It uses the backscattering of radio waves from acoustic wave fronts to measure the speed of sound. This sound speed is translated into the so called sonic temperature, which is very near to the virtual temperature (Kaimal and Gaynor, 1991) and therefore controlling the hydrostatic stability.

The principles of RASS technology were developed and demonstrated already four decades ago (e.g. Marshall et al., 1972; North et al., 1973; Nalbandian, 1977; Makarova, 1980), and systematic comparisons of RASS temperature profiles with

AMTD
5, 1075–1100, 2012

in-situ soundings, radiometric soundings or mast measurements were accomplished (e.g. Bonino et al., 1985; Angevine et al., 1998; Görsdorf, 1998; Argentini et al., 2008; Pérez et al., 2008). In the course of exploring the method two classes of RASS were defined, which use either the propagation time of the electromagnetic waves (Bragg-RASS) or of the acoustic waves (Doppler-RASS) for range discrimination (Peters et al., 1983). Various corrections have been developed which account for cross sensitivities to atmospheric parameters like horizontal and vertical wind, turbulence, stratification, and humidity as well as to geometric features of the radio and the acoustic antennas (Lataitis et al., 1993; Kon, 1985; Peters and Angevine, 1996; Petenko, 1999). While these corrections are common for both classes of RASS, a systematic distortion of low level temperature gradients especially observed with Bragg-RASS was successfully analyzed by Görsdorf and Lehmann (2000) and an efficient correction scheme was proposed.

Here we consider the Doppler-RASS, which is implemented as a supplement of Doppler-SODAR, and which is primarily used for sampling the lower few hundred meters of the atmosphere. These systems use typically separated antennas for the continuous transmission and the reception of radio waves (bi-static antenna configuration). This implies that the scattering angle becomes height dependent. Since the effect ist most pronounced at short ranges the usual far field approximation is not applicable for calculating the Doppler shift. The bi-static effect on the relation between Doppler shift and phase velocity of the acoustic waves has been analyzed theoretically by Kon (1981) and a first order near field correction has been derived. Among other approximations a Gaussian illumination distribution of the antenna apertures and isotropic acoustic transmission is assumed for the sake of mathematical convenience. Therefore an empirical adjustment of algorithm parameters needs to be applied in order to minimize the bias of RASS-derived temperatures at low altitudes.

This paper is organized as follows. The RASS and antenna configurations that were used in this study are described in the Sect. 2, the relation between Doppler shift and phase velocity according to Kon's approximation is introduced in Sect. 3, and the

AMTD
5, 1075–1100, 2012

empirical correction of this approximation is proposed in Sect. 4. Finally results from various measurement campaigns are presented and discussed in Sect. 5.

2 The RASS system

2.1 Basic principle

The sound velocity c_a is derived from the measured Doppler frequency shift δf of the backscattered electromagnetic signal. From the sound velocity the local air temperature can by inferred. Within ideal gas approximation the relation between the so called sonic temperature T_s and sound velocity is given by the numerical-value equation

$$\frac{T_s}{\mathrm{K}} = \left(\frac{c_a}{\mathrm{m\,s^{-1}}} \, \frac{1}{20.047} \right)^2 . \tag{1}$$

T_s is related to the temperature by

$$T_s = T \left(1 + 0.32 \frac{e}{p} \right) \tag{2}$$

with e water vapor partial pressure and p atmospheric pressure (Kaimal and Gaynor, 1991). T_s is very close to the virtual temperature T_v, namely $T_s = T_v \left(1 - 0.06\, e/p\right)$. Therefore, the gradient of T_s is a good proxy variable for the static stability of the atmosphere. A comprehensive introduction into the theory of RASS including various cross sensitivities and second order effects can be found in Lataitis (1992).

2.2 Integrated SODAR/RASS

For the measurements reported below a SODAR/RASS manufactured by METEK Ltd. (MERASS) was used. An electromagnetic continuous-wave transmitter at 1290 MHz and a corresponding receiver is installed adjacent to the SODAR-antenna. METEK-SODARs transmit sound pulses in cycles of up to 5 beam directions. This transmit

AMTD
5, 1075–1100, 2012

cycle is extended with an additional RASS-sound-pulse. The SODAR signal processing hardware handles the corresponding RASS receiving signal like an additional beam direction. Thus RASS- and SODAR-profiles can be measured in nearly any staggered order, such that after averaging of a larger number of cycles the mean RASS- and SODAR-profiles can be considered to be quasi-simultaneous. After mixing of the RASS receiving signal into the base band its properties are very similar to SODAR-echoes, such that the same hardware can be used for processing the SODAR- as well as the RASS-echoes. Thus, MERASS is a virtually integrated system for the simultaneous measurement of wind and temperature profiles. With MERASS the temperature profile is measured with a height resolution of down to 10 m starting at 35 m above the ground.

3 Bi-static correction

Due to the continuous operation of the electromagnetic transmitter the transmit and receiving antennas need to be separated as illustrated in Fig. 1. The distance between the antennas of MERASS is typically 4–6 m. Therefore the scattering angle is not exactly 180°, and it depends on height. Disregarding the bi-static deviation from backscattering would lead to a temperature bias in the order of 1 K at the lowest altitude, and it would vanish rapidly with increasing height. For some applications, as for example estimating the static stability, the temperature gradient is more important than the absolute temperature itself, and a height dependent bias would lead to significant misinterpretations.

For arbitrary scattering angles α the Doppler shift is given by

$$\delta f_{\mathrm{bi}} = 2 f_e \frac{c_a}{c_e} \sin\frac{\alpha}{2} \tag{3}$$

while for backscattering ($\alpha = 180^\circ$) we have

$$\delta f_{\mathrm{back}} = 2 f_e \frac{c_a}{c_e} \tag{4}$$

with c_e speed of light.

AMTD
5, 1075–1100, 2012

Disregarding the bi-static deviation means to retrieve c_a from Eq. (4) but using the Doppler shift δf_{bi}

$$c_a^* = c_a \sin\frac{\alpha}{2} \tag{5}$$

with c_a and c_a^* true and biased sound velocity respectively. With Eq. (1) we obtain for the bias and true temperature

$$T = T^* \left(\sin\frac{\alpha}{2}\right)^{-2}. \tag{6}$$

If the transmitter and receiver would be a point-source and -sink respectively, the scattering angle α, as indicated in Fig. 1, would be related to the measuring height h and the distance D between transmit- and receiving antenna according

$$\tan\alpha = -\frac{D}{2h}. \tag{7}$$

For scattering angles with small deviation from 180° Eq. (6) would then take the approximate form

$$T = T^* \left(1 + \frac{D^2}{4h^2}\right). \tag{8}$$

In reality the extension of the antenna apertures must not be neglected, particularly at low ranges. Here the wavefronts are not perfectly spherical as in the far field. Kon (1981) developed for this range a generalization of Eq. (8) which takes into account the extension of antenna apertures. For mathematical convenience he replaced the real illumination function of the antenna apertures by a rotation-symmetric Gaussian function, which depends only on the distance from the aperture center (see Fig. 2). The standard deviation of the Gaussian function is indicated by a_e and a dimensionless farfield parameter $Q_e = h/\left(k_e a_e^2\right)$ normalized with the wave number k_e is introduced.

AMTD
5, 1075–1100, 2012

Kon derived an approximate analytical expression for the bi-static bias analogue to Eq. (6) which accounts for terms up to the order Q_e^{-4} and which still assumes only small deviations from backscatter geometry. A further simplification is the assumption of an acoustic point source (isotropic).

$$T = T^* \left(1 + \frac{1}{4} \frac{D^2}{h^2} \frac{1 - Q_e^{-2}}{(1 + Q_e^{-2})^2} \right). \quad (9)$$

4 Proposed empirical correction

4.1 Effect of bi-static correction

Equation (9) does not in all cases give satisfactory results for the lower heights of a RASS temperature profile – even, if we restrict the analysis to heights where Eq. (9) should be applicable (i.e. $\alpha \approx 180^\circ$, $Q_e^2 \gg 1$. This has been found in comparisons with in situ measurements (Argentini et al., 2008), but also by assessing the coincidence between in-situ measured temperature profiles near the surface and the RASS-profiles wich start at 30 m or 40 m above ground. Equation (9) assumes a Gaussian illumination distribution of the antenna apertures, which has by definition an infinite extension, whereas a realistic illumination function is truncated at the physical rim of the aperture. Therefore there is some arbitraryness in the choice of a_e, and various approaches are imaginable. Similarly, the nominal separation of the antennas, defined by the distance of the (Gaussian) beam axes, may not provide the best correction with Kon's model.

We suggest therefore an empirical adaptation of a_e and D such that the RASS temperature profiles in the lower height levels fit best to "true" profiles.

The effect of different values of a_e and D on the temperature correction $T - T^*$ according Eq. (9) is illustrated in Fig. 3. In this figure, we assume a sound velocity of 340 m s^{-1} (corresponding 14.5 °C), a frequency of 1290 Mhz, and a physical antenna radius of 1 m. The colors indicate different choices of a_e between 0 and 1 m. For each a_e three choices of D are shown, as indicated on the corresponding line. A nominal

AMTD
5, 1075–1100, 2012

antenna separation of $D = 6$ m was assumed, and in addition, the graphs for ±0.5 m deviation from the nominal separation are plotted. These deviations may be attributed partly to model simplifications and partly to uncertainties of the antenna positioning. The left panel shows the temperature correction, and the right panel shows the corresponding correction of temperature gradient, if it is derived fom temperature differences between heights separated by 30 m.

We recognize (except of $a_e = 0$) a height of maximum correction which moves upward with increasing a_e. Although Kon (1981) did not provide an estimate of the residual correction related to the approximations of his model, we believe that the height of maximum bias is below the applicable height of Kon's model.

If we set a_e equal to the physical radius of the aperture ($a_e = 1$ m), the correction proposed by Kon (1981) results in a maximum temperature correction of only 0.52 K. Replacing the physical radius by a reduced effective radius $a_e < 1$ m increases the temperature correction, and shifts the lower border of the model to lower heights. This offers the possibility to adjust the temperature profile in the near range empirically by the choice of a_e. The sensitivity of the profile shape to D is comparably small for reasonble variations of D. Since the reference measurements available for this study were not sufficiently detailed to provide guidance for the choice of D, the nominal value of D was used here, and only a_e was varied for adaption to reference measurements.

4.2 Validation of bi-static correction

Applying the above mentioned correction with a changed effective radius to RASS temperature profiles, a solid validation by a reference profile is often not possible. But in most cases the RASS profiles are supplemented by near-surface measurements at 2 m and 10 m height which enables a plausibility examination of the constructed complete profile.

Here we analyse a measuring campaign at Munich Airport north of the city. The campaign took place from 23 June 2010 to 6 October 2010. The site is flat and undisturbed. RASS-temperature data are available every 10 min and the height levels are 40 m to

AMTD
5, 1075–1100, 2012

500 m with $\Delta h = 20$ m. The distance between the radar antennas is 6 m, and the physical radius of the antennas is 1 m. Near-surface temperature (Pt100-thermometer) and relative humidity were measured at 2 m and 10 m height synchronous to the RASS measurements to provide virtual temperature.

The effective radius a_e is set to a value of 0.8 m. Apparently, the correction is significant in the lower height ranges, and the corrected profiles appear to fit the near-surface profiles better, as Fig. 4 shows.

Also the temperature gradient seems to be more realistic as frequency distributions for the lowest two RASS levels and for elevated levels show (Fig. 5). Around noon, there is a clear shift at the lowest levels from mostly positive gradients, i.e. stable stratification (uncorrected) to more negative and near-zero gradients, i.e. neutral and unstable stratification (corrected). Around midnight, the gradients are shifted from strongly stable (uncorrected) to moderately stable stratification (corrected). This result seems to be plausible. At larger heights the correction nearly vanishes (Fig. 5, right).

Another plausibility test of the bi-static correction according Kon (1981) is the comparison with a simple empirical correction, which assumes near-neutral conditions – and thus adiabatic temperature profiles. In this approach we assume that this condition is satisfied for profiles measured between 10:00–18:00 UTC with wind speed exceeding 2 m s^{-1}. All temperature values T at heights below 100 m are converted locally to potential temperature Θ by $\Theta = T + h \cdot \gamma$ with $\gamma = 10^{-2}$ K m^{-1}. For all temperature profiles, which match the above conditions, the difference to the 100-m temperature is determined and averaged. The result is an empirical adiabatic correction for each height lower than 100 m. Assuming that this correction is not restricted to neutral conditions but generally valid it is applied to all data sets. Figure 6 shows the same two profiles as displayed in Fig. 4. The corrections below 100 m are nearly identical in both figures, which supports the bi-static correction being physically reasonable.

AMTD
5, 1075–1100, 2012

5 Application examples

We describe here boundary layer studies using corrected RASS temperature profiles and supplemented near-surface in-situ measurements.

5.1 Temperature profile evolution over flat terrain

The flat environment around Munich Airport was chosen for studying the diurnal boundary layer evolution into the lower troposphere up to 500 m. Figure 7 shows the evolution of potential temperature profiles over a 24 h period in July. During night time the near-surface temperature decreases continuously resulting in a very stable stratification, particularly around midnight. In the morning a very rapidly growing neutral boundary layer evolves with top height near 100 m at 07:00 UTC and above the RASS range of 350 m at 09:00 UTC. The stratification above 50 m remains neutral until 19:00 UTC, followed by cooling in the lower 50 m.

An explanation of this development can be given by simultaneous measurements of wind speed and sensible heat flux from the sonic anemometer/thermometer at 2 m height (Fig. 8). The night is rather calm with wind speed mostly lower than 1 m s^{-1}, and the low mixing results in a very stable stability. The depth of the stable layer cannot clearly be determined because it exceeds the range of the RASS. After 05:00 UTC sensible heat flux increases and warms the layer below 100 m until 17:00 UTC. With the onset of a stronger wind after 07:00 UTC a vertical mixing sets on and results in neutral profiles. The measuring range of the RASS is controlled by the combination of wind and turbulence (Kon, 1985) and remains lower than 400 m during daytime. The increased range of 500 m at 19:00 UTC is probably due to weakening of the wind in combination with residual turbulence.

5.2 Thermal structure of the valley atmosphere

The second location of RASS measurements is Jesenice in Slovenia. The Jesenice valley runs from 120° to 300° and the crest reaches up to 1000 m over the valley floor.

AMTD
5, 1075–1100, 2012

The meteorological situation is dominated either by a thermally induced mountain – valley wind regime in calm and sunny situations or by a dynamically induced flow through the valley in windy and overcast situations. The thermal structures of the valley atmosphere differ strongly between these situations.

Figure 9 (left) shows the temperature profiles during 24 h in a mountain – valley wind regime. While the morning and evening profiles exhibit stable stratification the profiles between 09:00 and 15:00 UTC are adiabatic. In contrast to the profile development over flat terrain (see Fig. 7) there is a rapid change in the regimes between 07:00 and 09:00 UTC and between 17:00 and 19:00 UTC. Warming and cooling is not coming from the surface but is happening over the whole lower valley atmosphere with the onset of another wind regime.

This is illustrated by the time-height plots of wind speed and wind direction in Fig. 10 (left). During the night time rather weak wind from 300 to 360° dominates. At about 06:00 UTC the valley wind sets on in 400 m and reaches the valley floor at about 08:30 UTC. In this time interval a strong warming can be recognized in the temperature profiles together with a mixing also due to larger wind speeds. At about 17:00 UTC the mountain wind sets on together with a stabilization of the temperature profiles.

A prevailing dynamical wind regime from 120 to 150° ("into the valley") can be observed on 24 October 2006 (Fig. 10, right). The temperature profiles (Fig. 9, right) show stable stratification and do not change much over the day until 19:00 UTC. Between 19:00 and 21:00 UTC temperature profile shifts by about 2 K to lower values over a height range of at least 300 m. This coincides with a change of the flow from "into the valley" to "out of the valley".

Thus the different wind regimes in a deep valley are accompanied by specific thermal regimes. As the stability in the lowest 300 m is crucial for air pollution issues, reliable temperature profile measurements are quite important.

AMTD
5, 1075–1100, 2012

5.3 Flux-gradient studies

During unstable conditions a linear correlation between the near-surface gradient of potential temperature and the surface sensible heat flux is expected. At larger heights where convective mixing dominates the local flux-gradient relation is no longer valid (Arya, 2005). The temperature profiles are close to neutral. During stable conditions the flux-gradient relations near the surface and aloft are much more complicated and are not considered here.

As an example for flux-gradient relationships temperature gradients at different heights and sensible heat fluxes are shown for two flat sites. The instrumented tower of the University Hamburg (http://wettermast-hamburg.zmaw.de/) is situated at Hamburg-Billwerder east of the city in the estuarine flat of the Elbe river. Temperature and heat flux data at heights from 2 m to 250 m are available for May and June 2003 with a time resolution of 10 min. At Toulouse (France) a measuring campaign with RASS (lowest measuring height is 40 m) and near-surface sonic (10 m) and profile measurements (2 m and 10 m) took place in an undisturbed environment from 1 May to 30 June 2005. Time resolution is 10 min.

The results can be seen in Fig. 11. At both sites the gradients at elevated heights are plotted against 10 m heat fluxes, too, because at Toulouse no other heights were available. A comparison of flux-gradient plots at various levels with data from equal heights and with 10 m-fluxes for Billwerder reveals nearly no differences. The surface layer can be treated as a constant flux layer.

A clear flux-gradient relation can be seen for positive heat fluxes at both sites in the lower panels of Fig. 11 representing the near-surface layer. The upper panels of Fig. 11 show the corresponding gradients measured at higher levels (50 m to 70 m in Billwerder, 40 m to 60 m in Toulouse). In Billwerder the temperature profiles are derived from in-situ sensors installed at the mast, whereas the upper level measurements in Toulouse were based on RASS. We see that the flux-gradient correlation becomes similarly weak at both sites. The RASS data show more scatter of the temperature

AMTD
5, 1075–1100, 2012

gradient in the unstable branch which can readily explained by the influence of turbulence on the retrieved sound velocity (no vertical wind correction has been applied). But apart from this difference the general structure of the regression is very similar to the in-situ data of Billwerder, which confirms the potential of RASS to provide realistic temperature gradients.

6 Conclusions

Temperature profiles measured by bi-static Doppler-RASS exhibit a bias in the near range, if the deviation from backscatter geometry is neglected. The correction according Kon (1981), considered here, takes into account the near field of the antennas, but it includes approximations and simplifications, which prevent the immediate application of the correction scheme. Here we studied the possibility of empirical tuning of the efficient antenna apertures in order to achieve best agreement with reality. For the considered RASS system an effective aperture radius of 0.8 of the physical radius was found to be optimal. This has been confirmed by comparison with near-surface in-situ measurenets and evaluation of temperature profiles under presumably adiabatic conditions. The potential of Doppler-RASS in combination with SODAR for continuous monitoring the diurnal development of the thermal and dynamic boundary layer structure in flat and complex topography as well as for the assessment of flux-gradient relations has been demonstrated by field measurements.

AMTD
5, 1075–1100, 2012

References

Angevine, W., Bakwin, P., and Davies, K.: Wind profiler ans RASS measurements compared with measurements from a 450-m-tall tower, J. Atmos. Ocean. Tech., 15, 818–825, 1998. 1077

Argentini, S., Pietroni, I., Gariazzo, C., Conidi, A., Mastrantonio, G., Pelliccioni, A., Petenko, I., Viola, A., and Amicarelli, A.: Temperature profiles by ground-based remote sensing and in situ measurements, IOP C. Ser. Earth Env., 1, 1–9, 2008. 1077, 1081

Arya, S.: Micrometeorology and atmospheric boundary layer, Pure Appl. Geophys., 162, 1721–1745, 2005. 1086

Bonino, G., Elisei, G., Marzorati, A., and Trivero, P.: Results on planetary boundary layer sounding by automatic RASS, Atmos. Res., 20, 309–316, 1985. 1077

Görsdorf, U.: About the accuracy of temperature measurements with rass, Meteorol. Z., 7, 241–247, 1998. 1077

Görsdorf, U. and Lehmann, V.: Enhanced accuracy of RASS-measured temperatures due to an improved range correction, J. Atmos. Ocean. Tech., 17, 406–416, 2000. 1077

Kaimal, J. C. and Gaynor, J. E.: Another look at sonic thermometry, Bound.-Lay. Meteorol., 57, 401–410, 1991. 1076, 1078

Kon, A.: A bistatic radar-acoustic atmospheric sounding system, Izv. Atmos. Ocean. Phys. (Engl. Transl.), 17, 481–484, 1981. 1077, 1080, 1082, 1083, 1087

Kon, A.: Combined effect of turbulence and wind on the signal intensity in radio-acoustic sounding of the atmosphere, Izv. Atmos. Ocean. Phys. (Engl. Transl.), 21, 942–947, 1985. 1077, 1084

Lataitis, R.: Theory and application of a radio-acoustic sounding system, Technical report, Ph.D. Thesis, University of Colorado, Boulder, Colorad, USA, 1992. 1078

Lataitis, R., Strauch, R. G., and Moran, K. P.: Temperature errors in rass caused by winds and turbulence, Proc. 26th Intl. Conf. on Radar Meteorol., 24–28 May 1993, Norman, OK, 1993. 1077

Makarova, T.: Measurement of temperature profiles by radio-acoustic sounding, Izv. Acad. Sci. USSR, Atmos. Oceanic Phys., 16, 118–120, 1980. 1076

Marshall, J. M., Peterson, A. M., and Barnes Jr., A. A.: Combined radar-acoustic sounding system, Appl. Optics, 11, 108–112, 1972. 1076

Nalbandian, O.: For the theory of radio-acoustic sounding of the atmosphere, Izv. Akad. Nauk,

AMTD
5, 1075–1100, 2012

USSR, Physics Atm. and Ocean., 13, 245–253, 1977. 1076
North, E., Peterson, A., and Parry, H.: RASS, a remote sensing system for measuring low-level temperature profiles, B. Am. Meteorol. Soc., 54, 912–919, 1973. 1076
Pérez, I., García, M., Sánchez, M., and de Torre, B.: Description of atmospheric variables measured with a RASS sodar: Cylces and distribution functions, J. Wind Eng. Ind. Aerod., 96, 436–453, 2008. 1077
Petenko, I. V.: Improved estimation of errors due to antenna geometry in rass based on a radar wind profiler, Meteor. Atmos. Phys., 71, 69–79, 1999. 1077
Peters, G. and Angevine, W.: On the correction of RASS temperature errors due to turbulence, Contrib. Atmos. Phys., 69, 81–96, 1996. 1077
Peters, G., Timmermann, H., and Hinzpeter, H.: Temperature sounding in the planetary boundary layer by RASS-system analysis and results, Int. J. Remote Sens., 4, 49–63, 1983. 1077

AMTD
5, 1075–1100, 2012

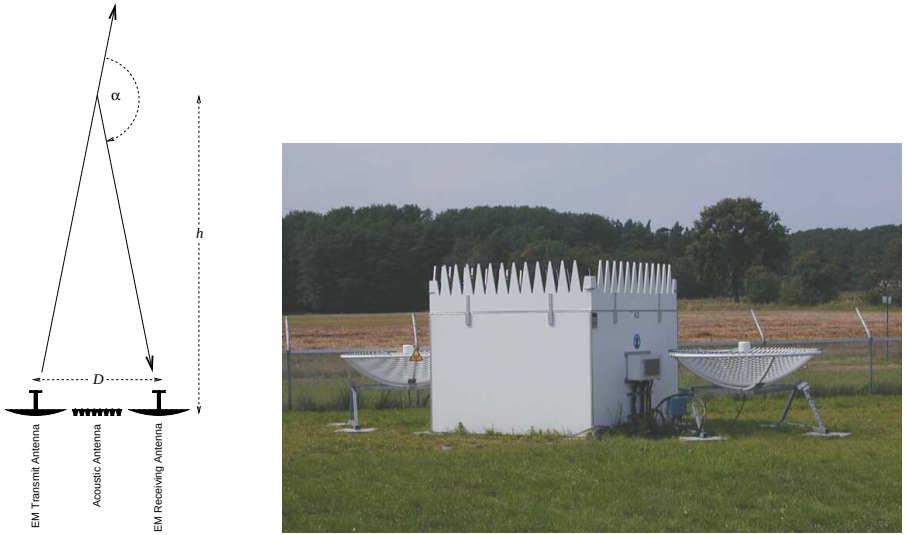

Fig. 1. Bi-static RASS antenna set up. α scattering angle, h measuring height, D distance between electromagnetic transmit and receiving antennas.

AMTD
5, 1075–1100, 2012

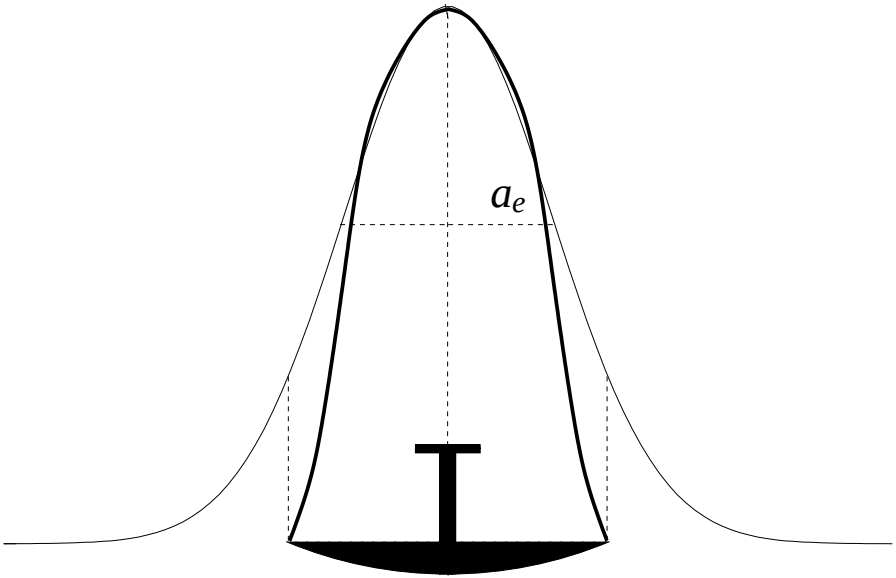

Fig. 2. Real (thick line) and modeled (thin line) Gaussian aperture illumination function with standard deviation a_e.

AMTD
5, 1075–1100, 2012

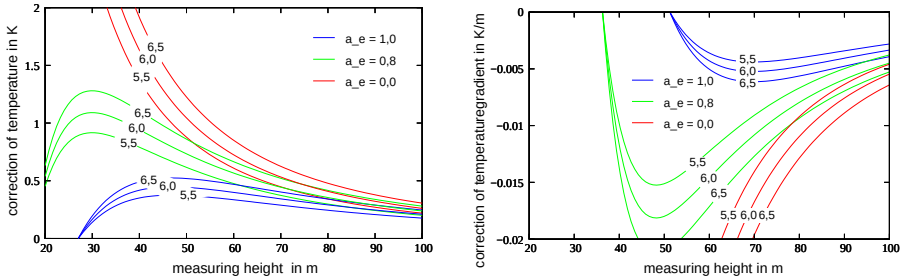

Fig. 3. RASS temperature correction versus height after Kon for different values of a_e and D. The line-color indicates a_e. For each color there are three lines, each representing a value of D as indicated in the lines. All lengths in m. The left panel shows the absolute temperature correction. The right panel shows the gradient correction, if it is derived from the temperature difference between two heights with 30 m separation centered around the indicated height.

AMTD
5, 1075–1100, 2012

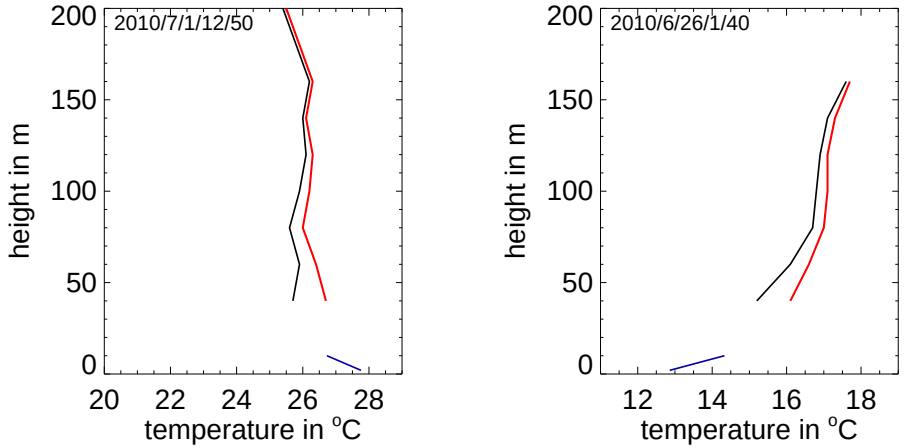

Fig. 4. Temperature profiles at Munich airport without (black) and with corrections (red).

AMTD
5, 1075–1100, 2012

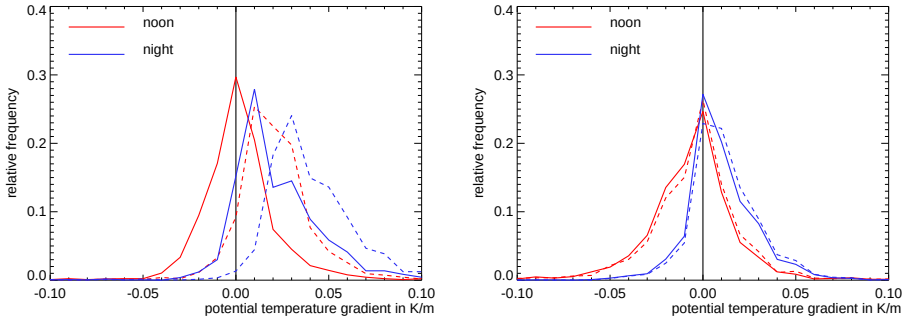

Fig. 5. Frequency distribution of quotient $\Delta T/\delta h$ at lowest height interval (60 m–40 m, left) and at elevated height interval (140 m–120 m, right) around noon and midnight for Munich. Dashed lines: uncorrected temperature, solid lines: corrected temperature.

AMTD
5, 1075–1100, 2012

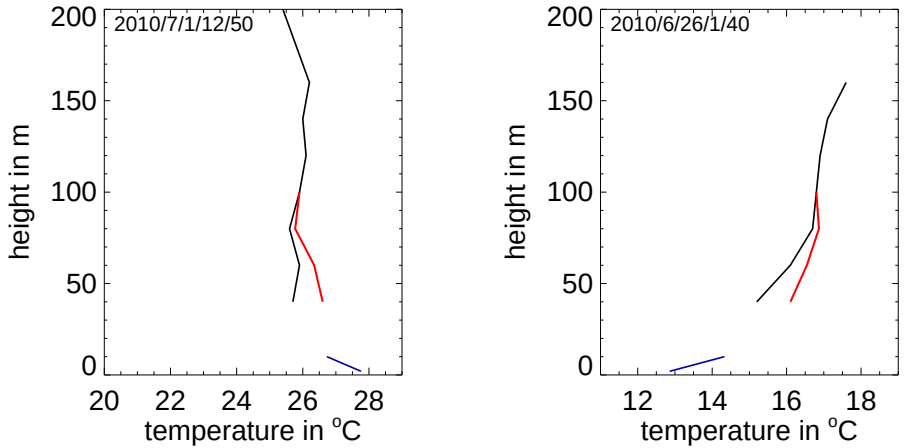

Fig. 6. Temperature profiles at Munich airport without (black) and with (red) empirical adiabatic corrections.

AMTD
5, 1075–1100, 2012

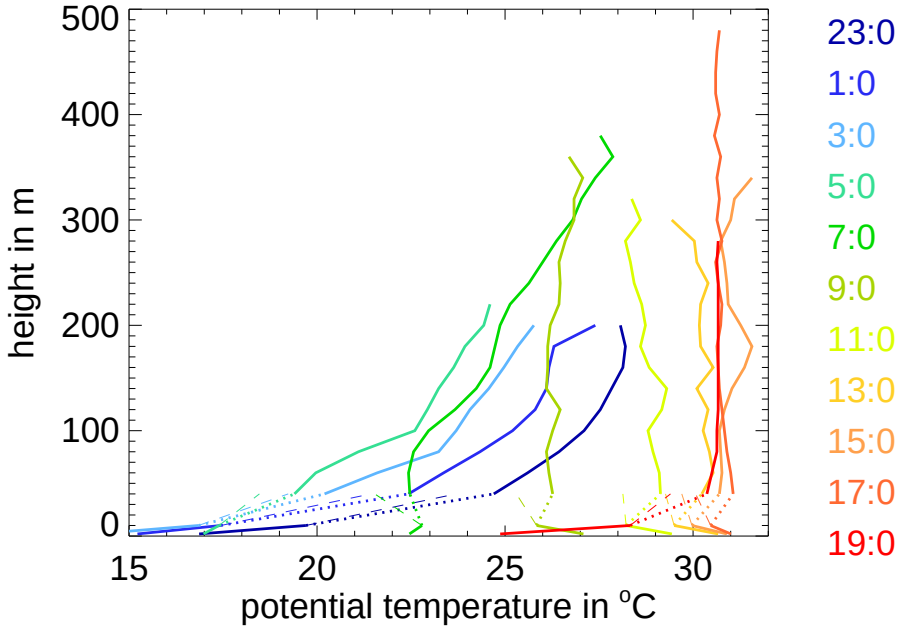

Fig. 7. Potential temperature profiles over 24 h at Munich airport on 2–3 July 2010.

AMTD
5, 1075–1100, 2012

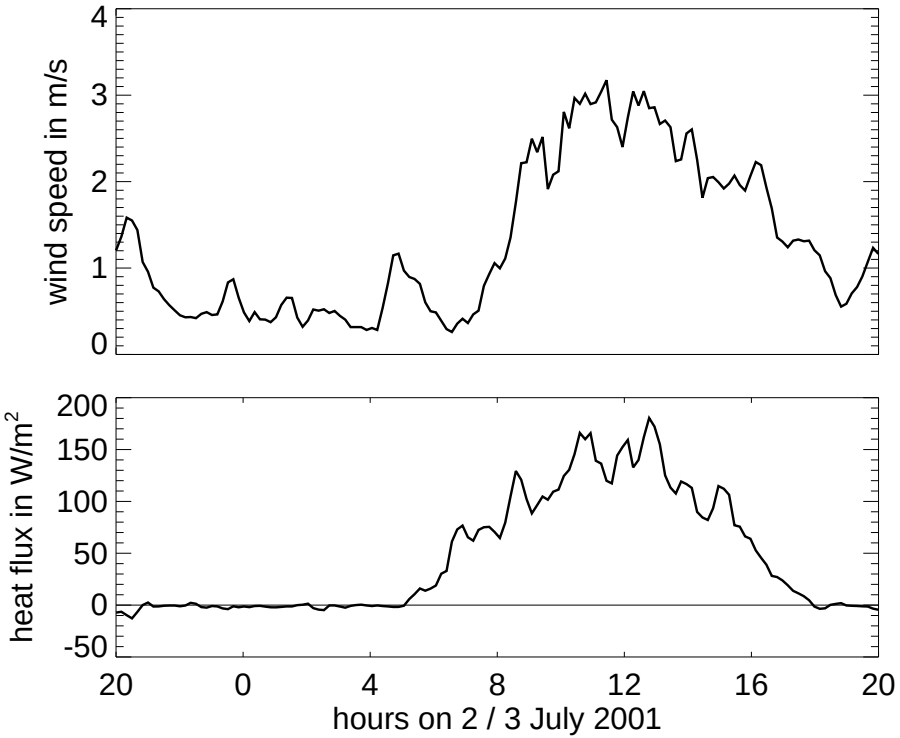

Fig. 8. Wind speed (top) and sensible heat flux (bottom) at 10 m height at Munich airport on 2–3 July 2010.

AMTD
5, 1075–1100, 2012

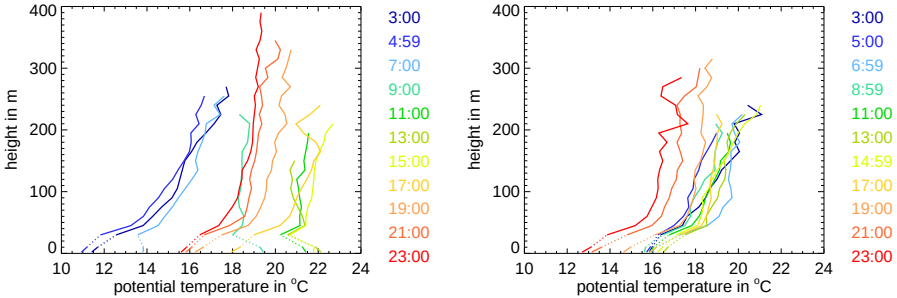

Fig. 9. Development of potential temperature profiles over 24 h at Jesenice on 21 September 2006 (left) and on 24 October 2006 (right).

AMTD
5, 1075–1100, 2012

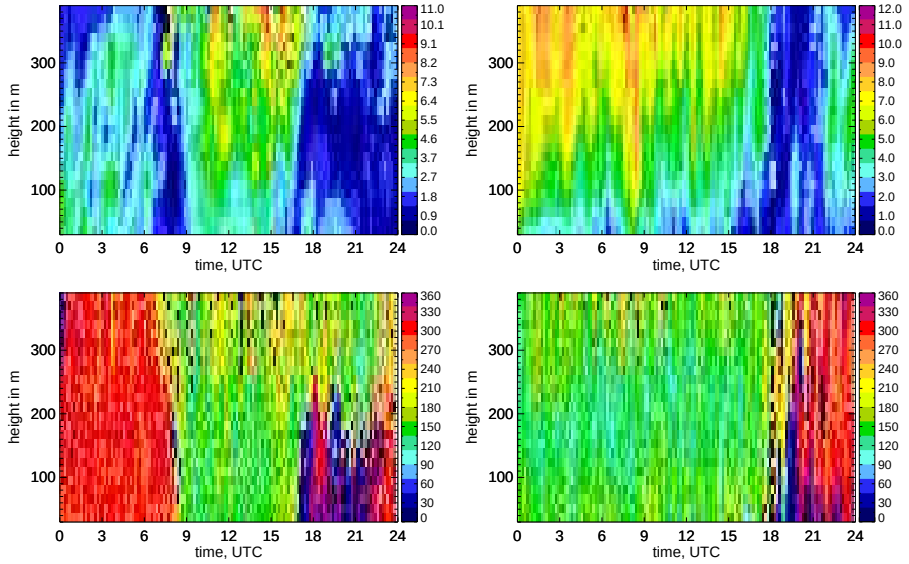

Fig. 10. Wind speed (top) and wind direction (bottom) at Jesenice on 21 September 2006 (left) and on 24 October 2006 (right).

AMTD
5, 1075–1100, 2012

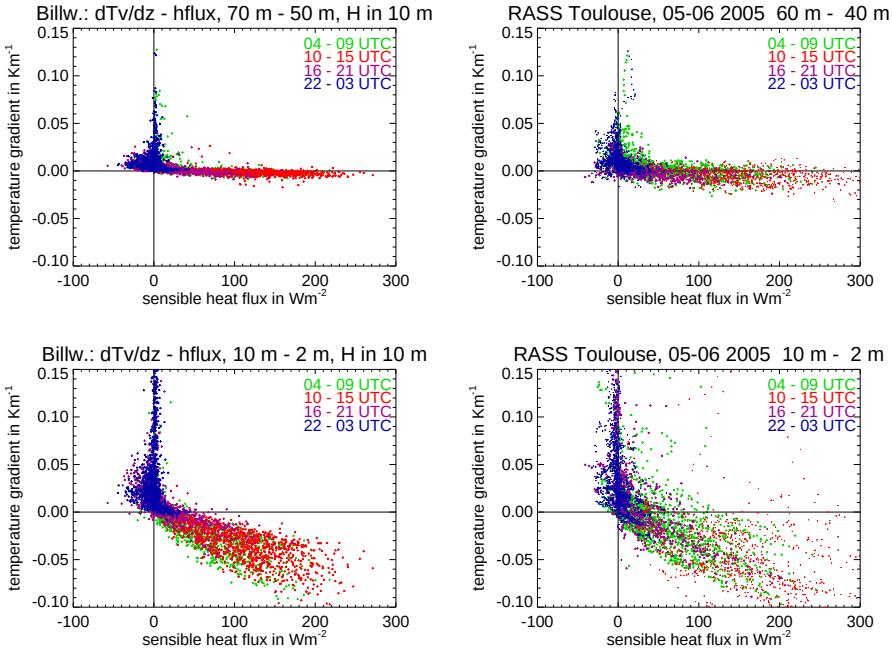

Fig. 11. Temperature gradients near the surface (bottom) and at elevated height (top) versus sensible heat flux at 10 m at Billwerder (left) and Toulouse (right).

AMTD
5, 1075–1100, 2012